

Disentangling X-ray dichroism and birefringence via high-purity polarimetry

Annika T. Schmitt,^{1,2,*} Yves Joly,³ Kai S. Schulze,^{1,2} Berit Marx-Glowna,² Ingo Uschmann,^{1,2}
Benjamin Grabiger,^{1,2} Hendrik Bernhardt,^{1,2} Robert Loetzsch,^{1,2} Amélie Juhin,⁴ Jérôme Debray,³
Hans-Christian Wille,⁵ Hasan Yavas,^{5,†} Gerhard G. Paulus,^{1,2} and Ralf Röhlsberger^{5,1,2,‡}

¹*Institut für Optik und Quantenelektronik, Friedrich-Schiller-Universität Jena, Max-Wien-Platz 1, 07743 Jena, Germany*

²*Helmholtz-Institut Jena, Fröbelstieg 3, 07743 Jena, Germany*

³*Institut Néel, 25 Rue des Martyrs, BP 166, 38042 Grenoble cedex 09, France*

⁴*Institut de Minéralogie, de Physique des Matériaux et de Cosmochimie (IMPMC), Sorbonne Université, UMR 7590, 4 place Jussieu, 75252 Paris Cedex 05, France*

⁵*Deutsches Elektronen-Synchrotron DESY, Notkestr. 85, 22607 Hamburg, Germany*

(Dated: July 1, 2022)

The advent of high-brilliance synchrotron radiation sources has opened new avenues for X-ray polarization analysis that go far beyond conventional polarimetry in the optical domain. With linear X-ray polarizers in a crossed setting remarkable polarization extinction ratios down to 10^{-10} can be achieved. This renders the method sensitive to probe tiniest optical anisotropies that would occur, for example, in strong-field QED due to vacuum birefringence and dichroism. Here we show that high-purity polarimetry can be employed to reveal electronic anisotropies in condensed matter systems with utmost sensitivity and spectral resolution. Taking CuO and La₂CuO₄ as benchmark systems, we present a full characterization of the polarization changes across the Cu K-absorption edge and their separation into dichroic and birefringent contributions, supported by calculations via an ab-initio quantum code. Our results not only pave the way for the precision detection of symmetry breaking interactions in correlated materials. At the upcoming diffraction-limited synchrotron radiation sources and X-ray lasers, where polarization extinction ratios of 10^{-12} can be achieved, our method has the potential to assess birefringence and dichroism of the quantum vacuum in fundamental studies of extreme electromagnetic fields.

Symmetries in nature are closely related to the fundamental structure of atoms, molecules and solids [1]. Symmetry breaking interactions in condensed matter, for example, form the fundamental basis for macroscopic quantum effects like magnetism, superconductivity, giant magnetoresistance, multiferroicity, and others, rendering the optical properties of such materials anisotropic. Access to symmetries and anisotropies of matter has been provided for centuries by optical effects like dichroism and birefringence [2], in particular by studying how the optical properties of matter depend on the polarization of light and how the polarization of light is affected by the interaction with matter. In recent decades, the use of highly brilliant X-rays from synchrotron radiation sources has provided access to the microscopic origins of magnetic and electronic anisotropies. This is facilitated, amongst others, via a suite of dichroic X-ray absorption spectroscopies in which the polarization dependence of X-ray absorption in the vicinity of atomic inner-shell transitions is monitored [3–7].

Polarization changes of X-rays in the interaction with matter occur not only due to absorptive but also through dispersive effects, leading to dichroism and birefringence, respectively. In the case of linearly polarized X-rays, dichroism causes a rotation of the polarization vector due

to an anisotropic absorption cross-section of the sample. X-ray birefringence results from different propagation velocities of two orthogonal polarization components, which leads to a phase shift between those and induces an ellipticity of the light. Both effects constitute sensitive probes for fundamental aspects of the light-matter interaction: In condensed matter physics, the spectral dependencies of X-ray dichroism and birefringence depict a very sensitive fingerprint of the electronic structure of the material. For example, tiny optical anisotropies emerging in the vicinity of phase transitions could reveal precursor mechanisms for structural transformations and electronic ordering in materials [8–10]. In quantum electrodynamics (QED) of extremely strong electromagnetic fields it is predicted that even the vacuum becomes optically anisotropic [11–14]. The resulting birefringence and dichroism could be sensitively probed by polarization analysis of hard X-rays after interaction with ultraintense light fields [15–17]. This would be a first test of nonlinear QED since the first considerations on this subject by Euler and Heisenberg in 1936 [18]. It is thus obvious that the precise detection of dichroic and birefringent polarization changes of scattered X-ray radiation would provide fundamental insights into condensed matter physics and QED effects alike. Motivated by these perspectives, very efficient high-purity polarimeters for hard X-rays have been developed with extinction ratios of up to 10^{-10} [19, 20]. They are based on two crossed linear Bragg polarizers between which the X-ray optical activity takes place [21–31].

In this Letter we show that these polarimeters with their

* annika.schmitt@uni-jena.de

† now at: SLAC National Accelerator Laboratory, 2575 Sand Hill Road, MS103, Menlo Park, CA 94025

‡ ralf.roehlsberger@desy.de

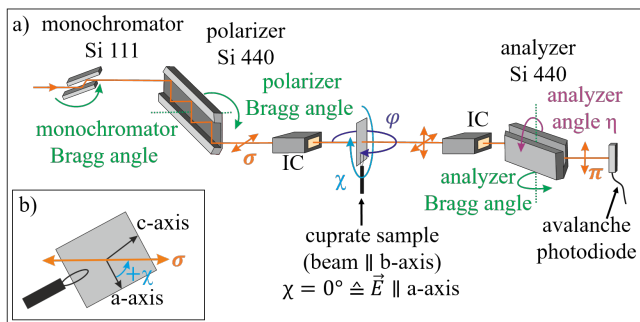


Figure 1. a) The sample was mounted on a Eulerian cradle with the b -axis parallel to the linearly polarized beam (σ - polarization in the horizontal plane). An avalanche photodiode behind the X-ray analyzer in crossed position to the polarizer detected the $\sigma - \pi$ scattered photons. Simultaneously ionization chambers (IC) measured the transmitted intensity through the sample. b) Enlarged view of the sample as seen from the direction of the incoming beam.

high energy resolution and excellent polarization purity allow to disentangle dichroism and birefringence with utmost sensitivity, consolidating the research field of spectroscopic polarimetry. We showcase the potential of this analysis technique by presenting a full characterization of the polarization changes across an atomic absorption edge and their separation into dichroic and birefringent contributions. As benchmark systems for correlated materials and parent compounds for cuprate superconductors, two materials have been chosen, CuO and La_2CuO_4 . We are probing the pronounced electronic anisotropies in these cuprate compounds that result from the particular symmetry of the Cu atom and its hybridizations with the surrounding orbitals in the near-edge region of the Cu K-absorption edge.

The experiments were performed at the synchrotron radiation source PETRA III (DESY, Hamburg) with the setup shown in Fig. 1a. A Si(111) heat-load monochromator selected a 1-eV wide energy band out of the incident radiation. The sample was located between two monolithic Si(440) channel-cut crystals, acting as highly efficient linear polarizers due to multiple reflections under the near- 45° Bragg angle for the X-ray energy of the Cu K-edge. In a 90° crossed setting, these two crystals form a polarimeter consisting of polarizer and analyzer [23], providing polarization extinction ratios of up to 10^{-10} [19] or better [32], which is way superior to what is possible in the regime of optical wavelengths. Any X-ray optical activity occurring between polarizer and analyzer converts a fraction of the highly pure σ - polarization incident on the sample into the orthogonal π - polarization that is then very efficiently transmitted by the analyzer and detected by an avalanche photodiode in single-photon counting mode. For precision angular adjustment relative to the incident beam, the sample was mounted on an Eulerian cradle, providing angular degrees of freedom along φ and χ .

The energy resolution of the X-ray polarimeter is determined by the Darwin width of the Si(440) polarizer and analyzer rocking curves which translates into an energy bandpass of 62 meV, thus allowing for the detection of very sharp spectral features. For scanning the polarimeter over the energy range of the Cu K-absorption edge with a constantly high polarization purity, the Bragg angles of polarizer and analyzer crystals have to be varied simultaneously with the Bragg angle of the Si(111) monochromator. According to the Bragg condition, the Bragg angle on the Si(440) plane has to be varied in an angular range from $\theta_B = 45.78^\circ$ to $\theta_B = 46.06^\circ$ to cover the energy range from 8970 eV to 9010 eV. In this energy range we achieved a polarization purity better than $1.3 \cdot 10^{-8}$, which was measured at 8970 eV and lies within the range between $1 \cdot 10^{-7}$ and $5 \cdot 10^{-9}$ that is predicted by the dynamical theory of X-ray diffraction.

To accurately determine the intensity of the $\sigma \rightarrow \pi$ scattered photons for a given polarimeter energy and angular setting (φ, χ) of the sample (see Fig. 1), the maximum of the rocking curve of the analyzer Bragg angle at each setting was taken. Fig. 2 shows the measured spectra of the $\sigma \rightarrow \pi$ scattered photons for both crystals in the setting $\varphi = 0$ as a function of the angle χ . By comparison with the conventional XANES spectra (see supplemental material [33] and the grey lines in Figs. 2e,j), one observes that in case of CuO, the $\sigma \rightarrow \pi$ scattering is maximal at the position of the pre-edge peak at 8984 eV, while in case of La_2CuO_4 this maximum occurs at the inflection point of the absorption edge at 8994 eV. These energy dependencies can be related to the Cu orbital configuration in the respective compound as will be discussed later.

The dependence of X-ray dichroism and X-ray birefringence on the photon polarization and the sample orientation is ruled by the point group of the crystal [34]. This is explained in detail in the supplemental material [33]. According to these considerations we chose the orientation $\varphi = 0$ for both sample materials, which corresponds to the electric field vector lying in the a - c -plane. This allows to detect the full anisotropy of the electric dipole absorption cross-section σ^D . Accordingly, the crystals were shaped into (010) - orientated slabs controlled by the Laue method with an accuracy of $\leq 0.3^\circ$. Subsequently they were gently polished to $33 \mu\text{m}$ (CuO) and $23.5 \mu\text{m}$ (La_2CuO_4) thin disks. The thickness of the samples was determined by transmission measurements and comparison to Henke data [35]. Finally, the adjustment of the crystal axes within the a - c plane was confirmed again by the Laue method.

For a description of the optical activity of these samples, i.e., the $\sigma \rightarrow \pi$ scattering, we use the complex linear absorption coefficient [36, 37]

$$\mu = \mu' + i\mu'' = \begin{pmatrix} \mu_{\sigma\sigma} & \mu_{\sigma\pi} \\ \mu_{\pi\sigma} & \mu_{\pi\pi} \end{pmatrix}, \mu_{xx} \in \mathbb{C}, \quad (1)$$

The real part μ' is responsible for dichroism, whereas the

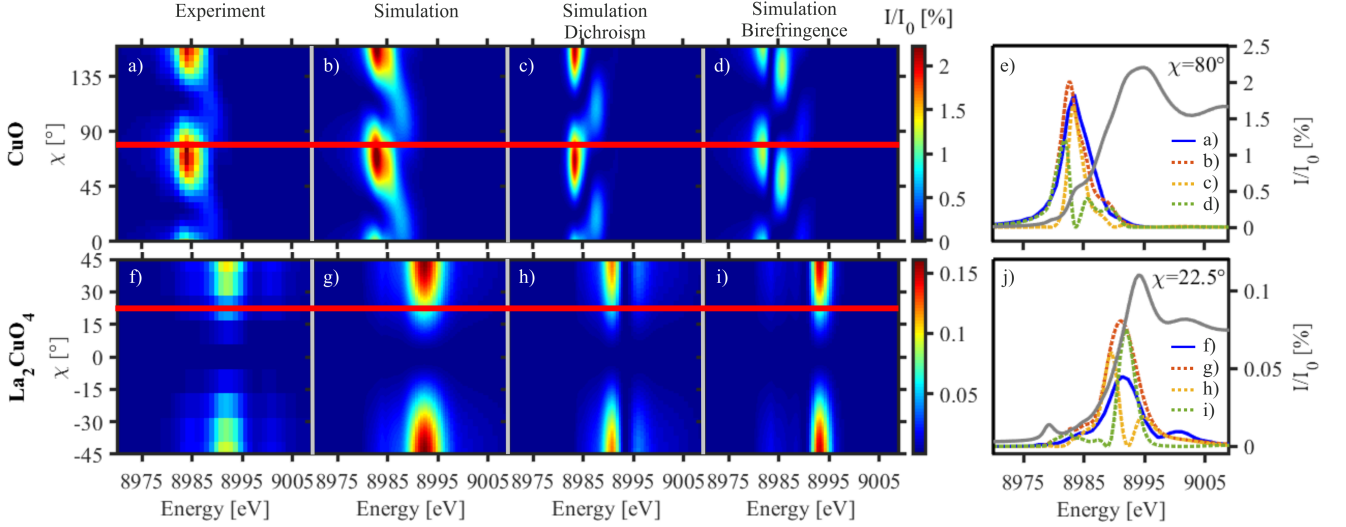


Figure 2. Intensity of the $\sigma \rightarrow \pi$ scattered photons of CuO (top) and La_2CuO_4 (bottom) normalized to the incident intensity I_0 on the sample for different angles χ between the crystal a -axis and the electric field vector. X-ray birefringence and dichroism were simulated by neglecting the anisotropic part of the real or imaginary part of the complex linear absorption coefficient μ , respectively. The red line in a) to d) and f) to i) marks the χ -position of the line out shown in e) and j), respectively. The corresponding XANES spectra are indicated in grey in e) and j).

imaginary part μ'' is related to birefringence.

In order to determine μ for the spectral region of the Cu K-edge of our samples, ab initio calculations were performed with the FDMNES code following the local density approximation [38]. The relativistic full potential approach was used, including spin-orbit interaction. Self-consistent electronic structures around the absorbing atom were calculated in a cluster with a radius of up to 6 Å. The code includes all calculation steps of the polarization changes in a material up to the final transmitted intensity after the analyzer.

For the calculation of polarization changes in the presence of a complex linear absorption coefficient, the Jones matrix formalism is used. The derivation is given in detail in the supplemental material [33]. Consequently, the π - polarized X-ray intensity after the sample normalized to the impinging σ - polarized X-ray intensity on the sample, $I_{\sigma\pi}$, is given by

$$I_{\sigma\pi} = e^{-\frac{1}{2}(\mu'_{\sigma\sigma} + \mu'_{\pi\pi})l} \frac{|\sinh(\tau l)|^2}{8|\tau|^2} \times \quad (2)$$

$$|(\mu_{\pi\pi} - \mu_{\sigma\sigma}) \sin 2\chi - 2\mu_{\sigma\pi} \cos 2\chi|^2,$$

where $\mu_{\sigma\pi} = \mu_{\pi\sigma}$ for centrosymmetric crystals, $\tau = \frac{1}{4}\sqrt{(\mu_{\pi\pi} - \mu_{\sigma\sigma})^2 + 4\mu_{\sigma\pi}\mu_{\pi\sigma}}$ [37, 39]. l is the thickness of the sample.

Based on this theoretical background, we will now discuss the influence of the symmetry of the complex linear absorption coefficient μ on the measured $\sigma \rightarrow \pi$ scattered intensity $I_{\sigma\pi}$. According to equation (2), the following behavior is expected: If the non-diagonal tensor elements $\mu_{\pi\sigma}$ are zero, $I_{\sigma\pi}$ is maximal at $\chi = \pm 45^\circ$ for all energies, since $I_{\sigma\pi}$ is then proportional to $\sin^2 2\chi$. If the

non-diagonal tensor elements $\mu_{\pi\sigma}$ are non-zero, the maxima of $I_{\sigma\pi}$ as a function of χ depend on the components of μ and thus are energy-dependent.

Both symmetry cases of the complex linear absorption coefficient μ were experimentally verified by investigating the two samples La_2CuO_4 ($\mu_{\pi\sigma} = 0$) and CuO ($\mu_{\pi\sigma} \neq 0$), as shown in Fig. 2. In agreement with the theory, all spectral features of La_2CuO_4 have the same angular dependence for which $I_{\sigma\pi}$ is maximum at $\chi = \pm 45^\circ$, whereas for CuO, there is an energy-dependent shift in χ for $I_{\sigma\pi}$ due to the nonzero $\mu_{\pi\sigma}$. Furthermore, $I_{\sigma\pi}$ has a χ - periodicity of $\pi/2$ for both crystals, which can easily be explained by their centrosymmetry. The theoretical simulation is in very good qualitative agreement with the experimental data. This is further exemplified by line cuts at selected χ angles shown in Figs. 2e, j. While the agreement in case of CuO is excellent, the deviation in the peak intensity for La_2CuO_4 might be due to a deviation of the crystal thickness from the nominal value.

The theoretical description also allows to calculate the spectra of the $\sigma \rightarrow \pi$ transmission separately for X-ray dichroism and X-ray birefringence. This can be achieved by neglecting the anisotropic part of either the real part or the imaginary part of μ , respectively, which is illustrated in Figs. 2c and 2d for CuO and Figs. 2h and 2i for La_2CuO_4 . It turns out that the total $\sigma \rightarrow \pi$ scattered intensity $I_{\sigma\pi}$ is the linear superposition of the $\sigma \rightarrow \pi$ scattered intensities due to X-ray dichroism and birefringence.

To verify this disentanglement of dichroism and birefringence experimentally, we have performed conventional X-ray linear dichroism measurements by taking XANES spectra for two orthogonal sample orien-

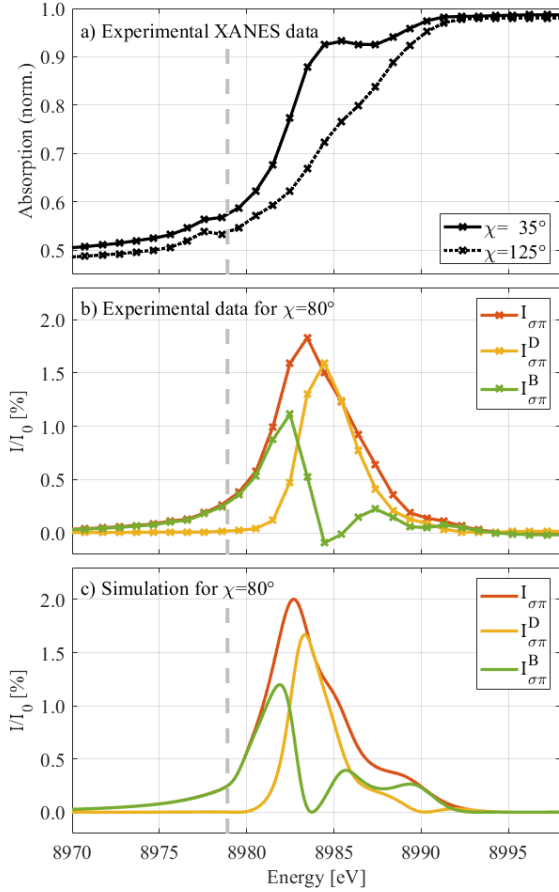


Figure 3. Experimentally disentangling dichroism and birefringence. a) The transmission ($= 1 - \text{absorption}$) through the sample at two orthogonal sample orientations $\chi \pm \frac{\pi}{4}$ is used to calculate the scattered intensity due to X-ray dichroism, $I_{\sigma\pi}^D(\chi)$, which can be subtracted from the total $I_{\sigma\pi}(\chi)$ to obtain the $\sigma \rightarrow \pi$ scattered intensity due to birefringence, $I_{\sigma\pi}^B(\chi)$, shown in b).c) Simulation with FDMNES. The dashed grey line marks the position of the Cu K-edge (8978.9 eV) according to Henke data [35].

tations. This is shown in Fig. 3a. For the calculation of the $\sigma \rightarrow \pi$ scattered intensity due to X-ray dichroism measured at the sample orientation χ , $I_{\sigma\pi}^D(\chi) = \frac{1}{2} \sin^2 \left[\frac{\pi}{4} - \arctan \left(\sqrt{\frac{T^+}{T^-}} \right) \right] \cdot (T^+ + T^-)$, the transmission through the sample, $T^\pm = T(\chi \pm \frac{\pi}{4})$, measured at the sample orientations $\chi \pm \frac{\pi}{4}$ is needed. This formula can be derived very easily by vector superposition and is explained in the supplemental material [33]. The $\sigma \rightarrow \pi$ scattered intensity due to X-ray birefringence can now be separated by a simple subtraction $I_{\sigma\pi}^B(\chi) = I_{\sigma\pi}(\chi) - I_{\sigma\pi}^D(\chi)$, which is plotted for $\chi = 80^\circ$ in Fig. 3b and is in excellent agreement with the simulated data shown in Fig. 3c.

The polarization changes due to dichroism and birefringence can be attributed to specific projections of the density of states on the absorbing atoms. In case of investigating a (010) - oriented sample with an X-ray beam

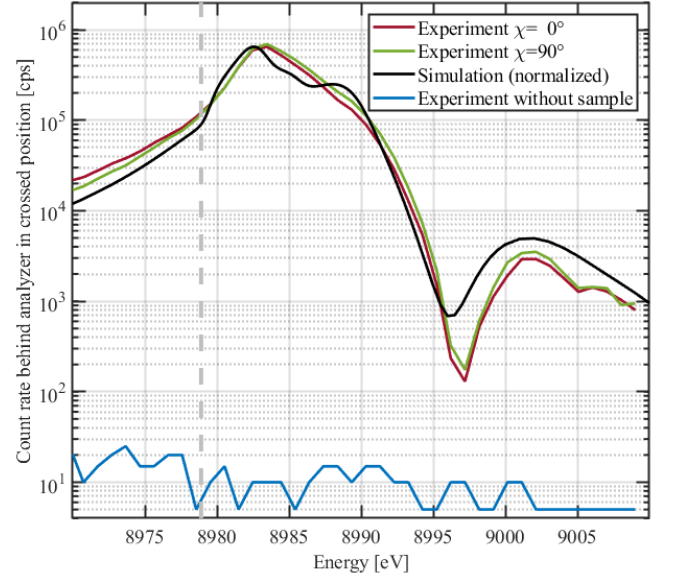


Figure 4. Intensity behind the analyzer in crossed position for $\chi = 0^\circ$ between the a -axis of the CuO crystal and the electric field vector of the beam. To demonstrate the reproducibility of the measurement, the data for $\chi = 90^\circ$ are also shown, which is in good agreement for the simulation over many orders of magnitude. The dashed grey line marks the position of the Cu K-edge (8978.9 eV) according to Henke data [35].

parallel to the crystal b -axis, the density of states $\delta(p_x)$, $\delta(p_z)$, $\delta(d_{xy})$ and $\delta(d_{yz})$ of the orbitals p_x , p_z , d_{xy} and d_{yz} are involved, where z is chosen along the c -axis of the crystal. $I_{\sigma\pi}$ is related to the difference between the density of states $\delta(p_x) - \delta(p_z)$ and $\delta(d_{xy}) - \delta(d_{yz})$. It turned out that $I_{\sigma\pi}^D$ is maximal, when $\delta(p_x) - \delta(p_z)$ is maximal, while $I_{\sigma\pi}^B$ is maximal for energies where $\delta(p_x) \approx \delta(p_z)$. This is illustrated in the supplemental material [33].

The analysis of $I_{\sigma\pi}$ has considerable advantages over conventional X-ray absorption measurements such as X-ray natural linear dichroism (XNLD): It is essentially background free and allows to monitor X-ray optical activity over a dynamic range of several orders of magnitude. Fig. 4 shows the $\sigma \rightarrow \pi$ transmission of the CuO sample for $\chi = 0^\circ$ and $\chi = 90^\circ$. This measurement not only proves the 90° periodicity of the anisotropy in this sample, but also highlights the excellent agreement with the theoretical simulation over almost four orders of magnitude. An energy scan that was performed without a sample in the beam illustrates the very low background level of the polarimeter. Thus, a dynamical range of six orders of magnitude and essentially background-free measurements enable unprecedented sensitivity to detect optical activity in the energy range of the Cu K-edge from 8970 eV to 9010 eV.

In conclusion, this Letter reports the first comprehensive experimental and theoretical investigation of X-ray birefringence and dichroism at the Cu K-edge for two different crystal systems. By measuring the X-ray dichroism

conventionally, the imaginary part of the complex linear absorption coefficient can be determined. The real part, which corresponds to X-ray birefringence, can be determined by subtracting the measured dichroism spectra from the $\sigma \rightarrow \pi$ scattered photon spectra. This is especially interesting for the determination of optical constants of materials that cannot be treated via ab initio calculations. Examples are materials that contain impurities like those that have been modified by ion implantation or doping, and those very strongly correlated systems, for which no suitable theoretical approach is currently capable of simulating their properties.

This method has several advantages over conventional methods for the detection of dichroism, such as XNLD, and can answer questions of fundamental importance. It can avoid the problem of integrating via a finitely measured absorption cross-section using the Kramers-Kronig relation in order to obtain the real part of the refractive index, which is the conventional approach. High polarization sensitivity is particularly suitable for observing small anisotropies as early indicators of phase transitions during or even long before reaching critical parameters. This new approach is especially interesting for investigating very weak anisotropies of quadrupolar or octopolar transitions in the pre-edge region like they were recently detected in $\text{Gd}_3\text{Ga}_5\text{O}_{12}$ at the Gd L_1 -absorption edge [40]. In contrast to XNLD, this method does not require spectra of orthogonal orientations to be subtracted from each other. Instead, the measurement of anisotropies with a high angular resolution is directly and quickly accessible. This enables single-shot measurements for

time-resolved investigations of certain spectral features in a pump-probe setting, for example. Furthermore, in analogy to an optical polarization microscope, it is also possible to image X-ray polarization anisotropies with very high spatial resolution.

Disentangling dichroism and birefringence with high sensitivity will also play a pivotal role in future experiments on probing QED in extreme electromagnetic fields with polarized X-rays. The experiments proposed so far [12–17] aim at the detection of the birefringence of the vacuum. A dichroic contribution to the signal would imply a correction to QED. It would, therefore, be a direct hint for the existence of particles beyond the standard model such as millicharged or axion-like particles [41, 42].

We would like to thank Heike Marschner and Ortrud Wehrhan for sharing their expertise in crystallography, and Claudia Rödl, Martin von Zimmermann, Paul Schenk and Felix Karbstein for helpful and enlightening discussions. This work was funded by the Deutsche Forschungsgemeinschaft (DFG) under Grant No. 416700351 within the Research Unit FOR2783/1, by the Bundesministerium für Bildung und Forschung (BMBF) under Grant No. 05K16SJ2 and by the European Social Fund (ESF) and the Free State of Thuringia in the framework of Forschergruppe 2017FGR0074. We acknowledge DESY (Hamburg, Germany), a member of the Helmholtz Association HGF, for the provision of experimental facilities. Parts of this research were carried out at PETRA III, and we would like to thank Ilya Sergeev, Hlynur Gretarsson, Rene Steinbrügge, Frank-Uwe Dill and Conrad Hagemeyer for assistance in using beamline P01.

-
- [1] L. D. Landau and E. M. Lifshitz, *Quantum Mechanics: Non-Relativistic Theory*, Course in Theoretical Physics (Butterworth-Heinemann, 1977).
- [2] M. Born and E. Wolf, *Principles of Optics* (Cambridge University Press, 1999).
- [3] D. H. Templeton and L. K. Templeton, *Acta Crystallographica Section A* **36**, 237 (1980).
- [4] B. T. Thole, G. van der Laan, and G. A. Sawatzky, *Phys. Rev. Lett.* **55**, 2086 (1985).
- [5] G. van der Laan, B. T. Thole, G. A. Sawatzky, J. B. Goedkoop, J. C. Fuggle, J.-M. Esteve, R. Karnatak, J. P. Remeika, and H. A. Dabkowska, *Phys. Rev. B* **34**, 6529 (1986).
- [6] G. Schütz, W. Wagner, W. Wilhelm, P. Kienle, R. Zeller, R. Frahm, and G. Materlik, *Phys. Rev. Lett.* **58**, 737 (1987).
- [7] L. Alagna, T. Prospero, S. Turchini, J. Goulon, A. Rogalev, C. Goulon-Ginet, C. R. Natoli, R. D. Peacock, and B. Stewart, *Phys. Rev. Lett.* **80**, 4799 (1998).
- [8] M. R. Norman, *Phys. Rev. B* **87**, 180506 (2013).
- [9] S. S. Pershoguba, K. Kechedzhi, and V. M. Yakovenko, *Phys. Rev. Lett.* **111**, 047005 (2013).
- [10] M. R. Norman, *Phys. Rev. B* **91**, 140505 (2015).
- [11] J. S. Heyl and L. Hernquist, *Journal of Physics A: Mathematical and General* **30**, 6485 (1997).
- [12] T. Heinzl, B. Liesfeld, K.-U. Amthor, H. Schwöerer, R. Sauerbrey, and A. Wipf, *Optics Communications* **267**, 318 (2006).
- [13] F. Karbstein, H. Gies, M. Reuter, and M. Zepf, *Phys. Rev. D* **92**, 071301 (2015).
- [14] F. Karbstein, *Phys. Rev. D* **98**, 056010 (2018).
- [15] F. Karbstein and C. Sundqvist, *Phys. Rev. D* **94**, 013004 (2016).
- [16] F. Karbstein and E. A. Mosman, “Enhancing quantum vacuum signatures with tailored laser beams,” (2020), [arXiv:2004.04268 \[quant-ph\]](https://arxiv.org/abs/2004.04268).
- [17] H.-P. Schlenvoigt, T. Heinzl, U. Schramm, T. E. Cowan, and R. Sauerbrey, *Physica Scripta* **91**, 023010 (2016).
- [18] W. Heisenberg and H. Euler, *Zeitschrift für Physik* **98**, 714 (1936).
- [19] B. Marx, K. S. Schulze, I. Uschmann, T. Kämpfer, R. Löttsch, O. Wehrhan, W. Wagner, C. Detlefs, T. Roth, J. Härtwig, E. Förster, T. Stöhlker, and G. G. Paulus, *Phys. Rev. Lett.* **110**, 254801 (2013).
- [20] H. Bernhardt, A. T. Schmitt, B. Grabiger, B. Marx-Glowna, R. Loetzsch, H.-C. Wille, D. Bessas, A. I. Chumakov, R. Ruffer, R. Röhlberger, T. Stöhlker, I. Uschmann, G. G. Paulus, and K. S. Schulze, *Phys.*

- Rev. Research **2**, 023365 (2020).
- [21] M. Hart, *Philosophical Magazine B* **38**, 41 (1978).
- [22] D. P. Siddons, M. Hart, Y. Amemiya, and J. B. Hastings, *Phys. Rev. Lett.* **64**, 1967 (1990).
- [23] M. Hart, D. P. Siddons, Y. Amemiya, and V. Stojanoff, *Review of Scientific Instruments* **62**, 2540 (1991).
- [24] D. P. Siddons, U. Bergmann, and J. B. Hastings, *Phys. Rev. Lett.* **70**, 359 (1993).
- [25] D. Siddons, J. Hastings, U. Bergmann, F. Sette, and M. Krisch, *Nucl. Instr. Meth. B* **103**, 371 (1995).
- [26] T. S. Toellner, E. E. Alp, W. Sturhahn, T. M. Mooney, X. Zhang, M. Ando, Y. Yoda, and S. Kikuta, *Applied Physics Letters* **67**, 1993 (1995).
- [27] R. Röhlberger, E. Gerdau, R. Ruffer, W. Sturhahn, T. Toellner, A. Chumakov, and E. Alp, *Nucl. Instr. Meth. A* **394**, 251 (1997).
- [28] E. Alp, W. Sturhahn, and T. Toellner, *Hyperfine Interactions* **125**, 45 (2000).
- [29] K. P. Heeg, H.-C. Wille, K. Schlage, T. Guryeva, D. Schumacher, I. Uschmann, K. S. Schulze, B. Marx, T. Kämpfer, G. G. Paulus, R. Röhlberger, and J. Evers, *Phys. Rev. Lett.* **111**, 073601 (2013).
- [30] K. P. Heeg, J. Haber, D. Schumacher, L. Bocklage, H.-C. Wille, K. S. Schulze, R. Loetzsch, I. Uschmann, G. G. Paulus, R. Ruffer, R. Röhlberger, and J. Evers, *Phys. Rev. Lett.* **114**, 203601 (2015).
- [31] J. Haber, K. S. Schulze, K. Schlage, R. Loetzsch, L. Bocklage, T. Gurieva, H. Bernhardt, H.-C. Wille, R. Ruffer, I. Uschmann, G. G. Paulus, and R. Röhlberger, *Nature Photonics* **10**, 445 (2016).
- [32] K. S. Schulze, *APL Photonics* **3**, 126106 (2018).
- [33] See Supplemental Material [url] for details on the theoretical description of the $\sigma \rightarrow \pi$ scattered intensity, the relation between the complex linear absorption coefficient and the atomic scattering factor, and on the conventional near-edge x-ray absorption spectra of CuO and La₂CuO₄, which includes Refs [36, 38, 39].
- [34] C. Brouder, *Journal of Physics: Condensed Matter* **2**, 701 (1990).
- [35] B. L. Henke, E. M. Gullikson, and J. C. Davis, *Atomic Data and Nuclear Data Tables* **54**, 181 (1993).
- [36] S. P. Collins, I. Dolbnya, B. A. Palmer, G. R. Edwards-Gau, A. Morte-Rdenas, B. M. Kariuki, G. K. Lim, K. D. M. Harris, and Y. Joly, *Journal of Physics: Conference Series* **425**, 132015 (2013).
- [37] Y. Joly, S. P. Collins, S. Grenier, H. C. N. Tolentino, and M. De Santis, *Phys. Rev. B* **86**, 220101 (2012).
- [38] Y. Joly, *Phys. Rev. B* **63**, 125120 (2001).
- [39] S. W. Lovesey and S. P. Collins, *Journal of Synchrotron Radiation* **8**, 1065 (2001).
- [40] A. Juhin, S. P. Collins, Y. Joly, M. Diaz-Lopez, K. Kvashina, P. Glatzel, C. Brouder, and F. de Groot, *Phys. Rev. Materials* **3**, 120801 (2019).
- [41] H. Gies, J. Jaeckel, and A. Ringwald, *Phys. Rev. Lett.* **97**, 140402 (2006).
- [42] L. Maiani, R. Petronzio, and E. Zavattini, *Physics Letters B* **175**, 359 (1986).

Disentangling X-ray dichroism and birefringence via high-purity polarimetry

Annika T. Schmitt,^{1,2,*} Yves Joly,³ Kai S. Schulze,^{1,2} Berit Marx-Glowna,² Ingo Uschmann,^{1,2}
 Benjamin Grabiger,^{1,2} Hendrik Bernhardt,^{1,2} Robert Loetzsch,^{1,2} Amélie Juhin,⁴ Jérôme Debray,³
 Hans-Christian Wille,⁵ Hasan Yavaş,^{5,†} Gerhard G. Paulus,^{1,2} and Ralf Röhlsberger^{5,1,2,‡}

¹*Institut für Optik und Quantenelektronik, Friedrich-Schiller-Universität Jena, Max-Wien-Platz 1, 07743 Jena, Germany*

²*Helmholtz-Institut Jena, Fröbelstieg 3, 07743 Jena, Germany*

³*Institut Néel, 25 Rue des Martyrs, BP 166, 38042 Grenoble cedex 09, France*

⁴*Institut de Minéralogie, de Physique des Matériaux et de Cosmochimie (IMPMC), Sorbonne Université, UMR 7590, 4 place Jussieu, 75252 Paris Cedex 05, France*

⁵*Deutsches Elektronen-Synchrotron DESY, Notkestr. 85, 22607 Hamburg, Germany*

(Dated: July 1, 2022)

SUPPLEMENTAL MATERIAL

A. Angular dependence of the X-ray absorption cross-section σ

The samples in this experiment belong to two different point groups:

- monoclinic CuO with point group $C_{2h}(2/m)$ and space group $C2/c$ ($a = 4.6837 \text{ \AA}$, $b = 3.4226 \text{ \AA}$, $c = 5.1288 \text{ \AA}$, and $\beta = 99.54^\circ$ [1]) and
- orthorhombic La_2CuO_4 with point group $D_{2h}(mmm)$ and space group $Bmab$ ($a = 5.352 \text{ \AA}$, $b = 5.400 \text{ \AA}$, $c = 13.157 \text{ \AA}$, and $\beta = 90^\circ$ [2]).

Both materials show trichroism, which means that all eigenvalues of the absorption cross-section tensor σ^D are different. The electronic transitions of CuO and La_2CuO_4 with the main absorption edge at approximately 8994 eV are mainly of electric dipole origin. The electric dipole absorption cross-section is given by

$$\sigma^D(\hat{\epsilon}) = \sigma^D(0,0) - \sqrt{\frac{8\pi}{5}} \sum_{m=-2}^2 Y_2^{m*}(\hat{\epsilon}) \sigma^D(2,m) \quad (1)$$

which depends (a) on the polarization vector $\hat{\epsilon}$ and the sample orientation relative to the photon wavevector through the spherical harmonics Y_l^m and (b) on the point group of the crystal and the photon energy through the tensor σ^D of the dipole absorption cross-section, with the complex tensor components $\sigma^D(l,m)$ [3], where m and l are the angular momentum quantum numbers. $\sigma^D(0,0)$ is the isotropic part of the electric dipole absorption cross-section which is independent of the polarization. The polarization vector $\hat{\epsilon} = [\sin(\chi - \beta) \cos \varphi, \sin(\chi - \beta) \sin \varphi, \cos(\chi - \beta)]$ is chosen in accordance with the experimental setup where χ represents the angle between the a -axis of the crystal and the electric field vector of the synchrotron beam as shown in Fig. 1b. For $\chi = 0^\circ$, the electric field vector is parallel to the a -axis. β is the base angle of the crystal lattice which is $\neq 90^\circ$ for the oblique lattice of monoclinic CuO.

In the case of CuO with point group $C_{2h}(2/m)$, where $\sigma^D(2,1) = \sigma^D(2,-1) = 0$, the electric dipole absorption cross-section is given by

$$\begin{aligned} \sigma^D(\hat{\epsilon}) = & \sigma^D(0,0) - \sqrt{3} \sin^2(\chi - \beta) [\cos 2\varphi \text{Re}\{\sigma^D(2,2)\} + \sin 2\varphi \text{Im}\{\sigma^D(2,2)\}] \\ & - \frac{1}{\sqrt{2}} [3 \cos^2(\chi - \beta) - 1] \sigma^D(2,0). \end{aligned} \quad (2)$$

For La_2CuO_4 with point group $D_{2h}(mmm)$, where $\sigma^D(2,1) = \sigma^D(2,-1) = 0$ and $\sigma^D(2,2) = \sigma^D(2,-2)$, $\sigma^D(\hat{\epsilon})$ is simplified to

* annika.schmitt@uni-jena.de

† now at: SLAC National Accelerator Laboratory, 2575 Sand Hill Road, MS103, Menlo Park, CA 94025

‡ ralf.roehlsberger@desy.de

$$\sigma^D(\hat{\epsilon}) = \sigma^D(0, 0) - \sqrt{3} \sin^2(\chi - \beta) \cos 2\varphi \operatorname{Re}\{\sigma^D(2, 2)\} - \frac{1}{\sqrt{2}} [3 \cos^2(\chi - \beta) - 1] \sigma^D(2, 0). \quad (3)$$

B. Theoretical description of $\sigma - \pi$ scattered intensity

We use the (2×2) Jones Matrix defined in a (σ, π) basis, σ horizontal, π vertical, and the wave vector k perpendicular to this basis.

1. Transmittance matrix

We use the transmittance matrix under the $\sigma - \pi$ basis where σ and π are 2 directions perpendicular to the wave vector. We note μ the complex linear absorption coefficient. Following Lovesey and Collins [4], after a distance l , the transmittance matrix is given by:

$$T(l) = e^{-\frac{1}{4}(\mu_{\sigma\sigma} + \mu_{\pi\pi})l} \begin{pmatrix} \cosh(\tau l) + \frac{\mu_{\pi\pi} - \mu_{\sigma\sigma}}{4\tau} \sinh(\tau l) & -\frac{\mu_{\sigma\pi}}{2\tau} \sinh(\tau l) \\ -\frac{\mu_{\pi\sigma}}{2\tau} \sinh(\tau l) & \cosh(\tau l) + \frac{\mu_{\sigma\sigma} - \mu_{\pi\pi}}{4\tau} \sinh(\tau l) \end{pmatrix} \quad (4)$$

$$\text{with } \tau = \frac{1}{4} \sqrt{(\mu_{\pi\pi} - \mu_{\sigma\sigma})^2 + 4\mu_{\sigma\pi}\mu_{\pi\sigma}} = \frac{1}{4}(\mu_{\pi\pi} - \mu_{\sigma\sigma}) \sqrt{1 + \frac{4\mu_{\sigma\pi}\mu_{\pi\sigma}}{(\mu_{\pi\pi} - \mu_{\sigma\sigma})^2}}$$

2. Polarization matrix

In the following we also use the Jones matrix for the polarization:

$$P = \frac{1}{2} \begin{pmatrix} 1 + S_1 & S_2 - iS_3 \\ S_2 + iS_3 & 1 - S_1 \end{pmatrix}. \quad (5)$$

When rotating the sample by an angle χ the linear polarization gets an angle $-\chi$ versus its σ direction. Thus one has:

$$S_1 = \cos 2\chi, S_2 = -\sin 2\chi, S_3 = 0 \quad (6)$$

$$P = \frac{1}{2} \begin{pmatrix} 1 + \cos 2\chi & -\sin 2\chi \\ -\sin 2\chi & 1 - \cos 2\chi \end{pmatrix} = \begin{pmatrix} \cos^2 \chi & -\sin \chi \cos \chi \\ -\sin \chi \cos \chi & \sin^2 \chi \end{pmatrix}. \quad (7)$$

3. Analyzer matrix

The analyzer matrix (or polarizer after the sample) is given versus its rotation angle, η , and its Bragg angle, θ , by:

$$A = \begin{pmatrix} \cos \eta & -\sin \eta \\ \cos 2\theta \sin \eta & \cos 2\theta \cos \eta \end{pmatrix}. \quad (8)$$

For a perfect analyzer crystal $\cos 2\theta = 0$. For the polarization flip by 90° , one then obtains:

$$A = \begin{pmatrix} \cos(-\frac{\pi}{2} + \chi) & -\sin(-\frac{\pi}{2} + \chi) \\ 0 & 0 \end{pmatrix} = \begin{pmatrix} \sin \chi & \cos \chi \\ 0 & 0 \end{pmatrix}. \quad (9)$$

4. Transmitted intensity

After the path through the sample, the intensity is given by

$$I = Tr(ATPT^\dagger A^\dagger) = |\sin \chi \cos \chi (T_{\sigma\sigma} - T_{\pi\pi}) + \cos^2 \chi T_{\pi\sigma} - \sin^2 \chi T_{\sigma\pi}|^2 \quad (10)$$

Non-diagonal non-magnetic case $T_{\sigma\pi} = T_{\pi\sigma}$:

$$I = |\sin \chi \cos \chi (T_{\sigma\sigma} - T_{\pi\pi}) + \cos 2\chi T_{\pi\sigma}|^2 \quad (11)$$

$$\begin{pmatrix} T_{\sigma\sigma} & T_{\sigma\pi} \\ T_{\pi\sigma} & T_{\pi\pi} \end{pmatrix} = e^{-\frac{1}{4}(\mu_{\sigma\sigma} + \mu_{\pi\pi})l} \begin{pmatrix} \cosh(\tau l) + \frac{\mu_{\pi\pi} - \mu_{\sigma\sigma}}{4\tau} \sinh(\tau l) & -\frac{\mu_{\sigma\pi}}{2\tau} \sinh(\tau l) \\ -\frac{\mu_{\pi\sigma}}{2\tau} \sinh(\tau l) & \cosh(\tau l) + \frac{\mu_{\sigma\sigma} - \mu_{\pi\pi}}{4\tau} \sinh(\tau l) \end{pmatrix}, \quad (12)$$

$$\begin{aligned} I &= e^{-\frac{1}{2}(\mu'_{\sigma\sigma} + \mu'_{\pi\pi})l} \left| \sin \chi \cos \chi \left(\frac{\mu_{\pi\pi} - \mu_{\sigma\sigma}}{2\tau} \sinh(\tau l) \right) - \cos 2\chi \frac{\mu_{\sigma\pi}}{2\tau} \sinh(\tau l) \right|^2 \\ &= e^{-\frac{1}{2}(\mu'_{\sigma\sigma} + \mu'_{\pi\pi})l} \frac{|\sinh(\tau l)|^2}{8|\tau|^2} |(\mu_{\pi\pi} - \mu_{\sigma\sigma}) \sin 2\chi - 2\mu_{\sigma\pi} \cos 2\chi|^2 \end{aligned} \quad (13)$$

with

$$\tau = \frac{1}{4} \sqrt{(\mu_{\pi\pi} - \mu_{\sigma\sigma})^2 + 4\mu_{\sigma\pi}\mu_{\pi\sigma}} \quad (14)$$

C. Derivation of the relation between complex linear absorption coefficient, complex refractive index and complex atomic scattering factor

A plane wave described by

$$E(z, t) = E_0 e^{i(kz - \omega t)} \quad (15)$$

passes through a medium with complex refractive index $n = 1 - \delta + i\beta = \frac{c \cdot k}{\omega}$:

$$E(z, t) = E_0 e^{i[\frac{\omega}{c}(1 - \delta + i\beta)z - \omega t]} \quad (16)$$

$$= E_0 e^{i\omega(\frac{z}{c} - t)} \cdot e^{-\frac{2\pi}{\lambda}(i\delta + \beta)z}. \quad (17)$$

By introducing the complex linear absorption coefficient $\mu = \mu' + i\mu''$, following S.P. Collins et al. [5], the expression can be written as

$$E(z, t) = \tilde{E}_0 \cdot e^{-\mu \frac{z}{2}} \quad (18)$$

with the vacuum propagation $\tilde{E}_0 = E_0 e^{i\omega(\frac{z}{c} - t)}$. This leads to the BeerLambert law for the intensity $I = |E|^2$:

$$I = I_0 e^{-\mu' z}. \quad (19)$$

A comparison of eq. 17 and eq. 18 shows that the complex linear absorption coefficient $\mu = \mu' + i\mu''$ is connected to the refractive index $n = 1 - \delta + i\beta$ via

$$\mu' = \frac{4\pi}{\lambda} \beta \text{ and} \quad (20)$$

$$\mu'' = \frac{4\pi}{\lambda} \delta. \quad (21)$$

Since the complex refractive index n can also be expressed by using the complex atomic scattering factor $f = f' - if''$,

$$n = 1 - \frac{n_a r_e \lambda^2}{2\pi} (f' - if'') = 1 - \delta + i\beta, \quad (22)$$

where n_a is the atomic density and r_e is the classical electron radius, there is also a relation between the complex linear absorption coefficient and the complex atomic scattering factor:

$$\mu' = 2n_a r_e \lambda f'' \quad (23)$$

$$\mu'' = 2n_a r_e \lambda f'. \quad (24)$$

D. X-ray absorption near edge structure of CuO and La₂CuO₄

The absorption cross-section was simulated for CuO (Fig. 1a) and La₂CuO₄ (Fig. 1c) with the ab-initio quantum code FDMNES in units of Mbarn ($1 \text{ Mbarn} = 10^{-18} \text{ cm}^2$) for different angles χ between the electric field vector and the a – axis of the crystal [6]. It was also determined experimentally by measuring the transmission through the sample with ionization chambers for CuO (Fig. 1b) and La₂CuO₄ (Fig. 1d). The main absorption edge (white line) is at approximately 8994 eV.

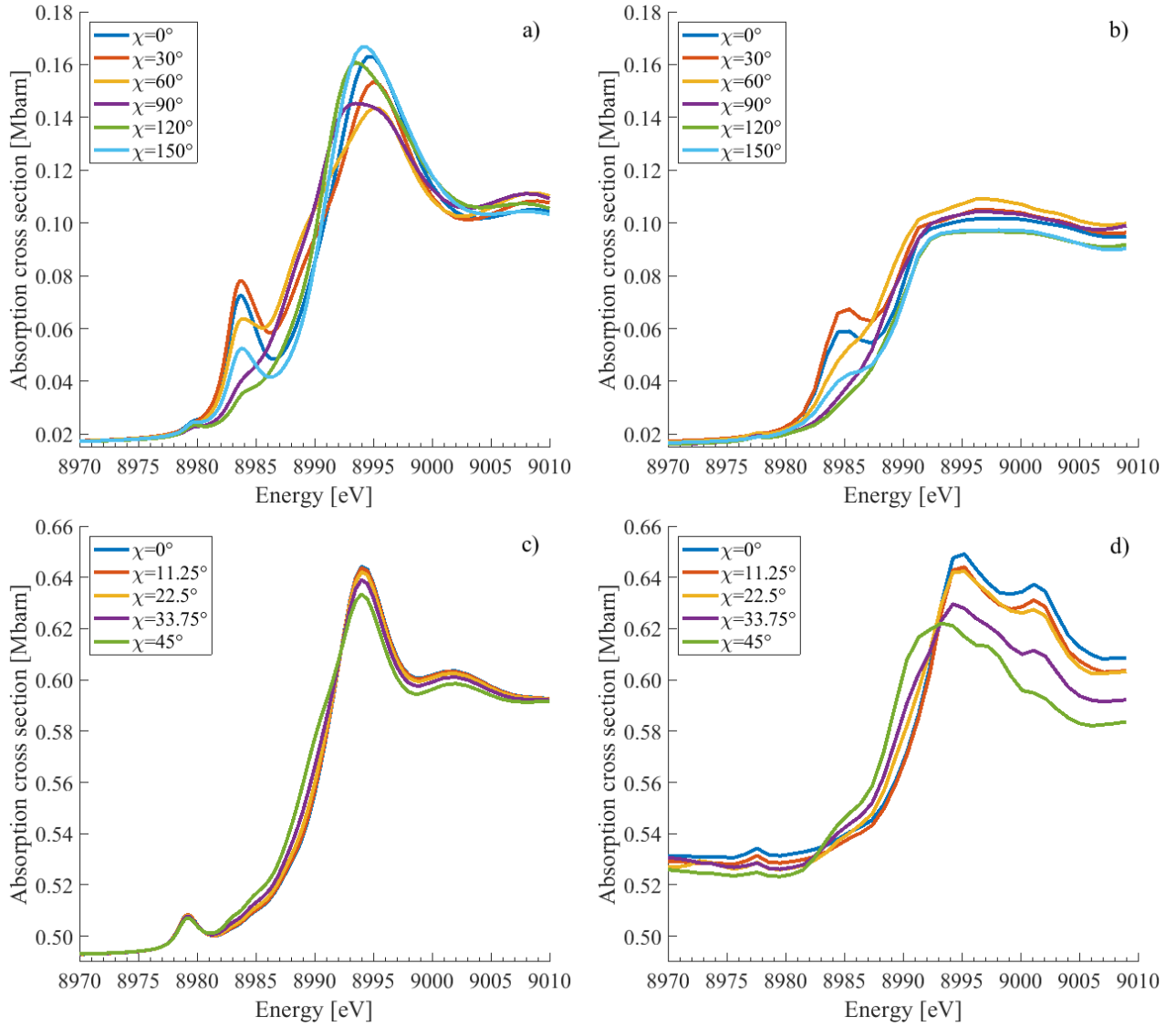


Figure 1. X-ray absorption near edge structure (XANES) simulated for CuO (a) and for La₂CuO₄ (c) for different sample orientations χ . Experimental data for CuO and La₂CuO₄ are shown in (b) and (d), respectively.

E. Calculation of the $\sigma \rightarrow \pi$ scattered intensity due to X-ray dichroism

The $\sigma \rightarrow \pi$ scattered intensity due to X-ray dichroism can be calculated using experimental XANES data, which are measured by ionization chambers before and behind the sample. Two orthogonal transmission measurements at the sample orientations $\chi \pm \frac{\pi}{4}$ are needed to calculate the $\sigma \rightarrow \pi$ scattered intensity due to X-ray dichroism at the sample orientation χ , which is normalized to the incident intensity I_{in} . The incoming electric field vector E_{in} is rotated by an angle $\Delta\chi$ due to dichroism in the sample, i.e. the different transmission of the electric field, t , at the sample orientations $\chi \pm \frac{\pi}{4}$:

$$\Delta\chi = \frac{\pi}{4} - \arctan\left(\frac{t(\chi + \frac{\pi}{4})}{t(\chi - \frac{\pi}{4})}\right) \quad (25)$$

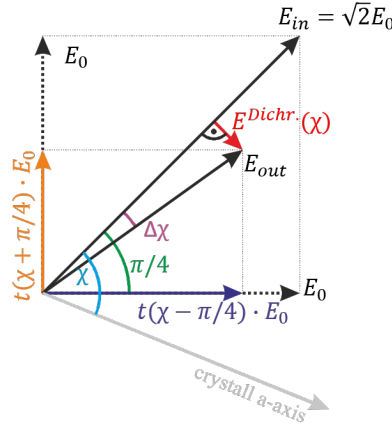


Figure 2. The incident electric field vector E_{in} is rotated by an angle $\Delta\chi$ due to the different transmission along the two orthogonal axis at the sample orientations $\chi \pm \frac{\pi}{4}$. The outgoing electric field vector E_{out} is no longer purely σ – polarized, but has now a π – component, $E^{Dichr.}(\chi)$, which can pass the X-ray analyzer in crossed position to the polarizer. The $\sigma \rightarrow \pi$ scattered photons due to X-ray dichroism at the sample orientation χ , $E^{Dichr.}(\chi)$, can be easily calculated when the transmitted intensity at the sample orientations $\chi \pm \frac{\pi}{4}$, $t^2(\chi \pm \frac{\pi}{4}) \cdot E_0^2$, is measured simultaneously with ionization chambers before and behind the sample, while the sample is rotated.

The incident electric field vector E_{in} is σ – polarized. The outgoing electric field vector

$$E_{out} = \left[t^2\left(\chi + \frac{\pi}{4}\right) \cdot E_0^2 + t^2\left(\chi - \frac{\pi}{4}\right) \cdot E_0^2 \right]^{1/2} \quad (26)$$

is rotated and therefore has also a π – polarization component, which can pass the analyzer in crossed position to the polarizer and is measured behind the analyzer as $\sigma \rightarrow \pi$ scattered photons $E^{Dichr.}(\chi)$. This can be calculated by

$$E^{Dichr.}(\chi) = \sin \Delta\chi \cdot E_{out} \quad (27)$$

The $\sigma \rightarrow \pi$ scattered intensity due to dichroism, $E_{Dichr.}^2(\chi)$, is normalized to the incident intensity $I_{in} = (\sqrt{2}E_0)^2$:

$$I_{\sigma\pi}^D(\chi) = \frac{E_{Dichr.}^2(\chi)}{(\sqrt{2}E_0)^2} = \frac{1}{2} \sin^2 \left[\frac{\pi}{4} - \arctan \left(\sqrt{\frac{T^+}{T^-}} \right) \right] \cdot (T^+ + T^-) \quad (28)$$

with the transmitted intensity $T^\pm = T(\chi \pm \frac{\pi}{4}) = t^2(\chi \pm \frac{\pi}{4})$.

F. Density of states of CuO and La₂CuO₄

The density of states were simulated with FDMNES. z was chosen along c – axis of the crystal. For a (010)-oriented sample and a beam along the crystal b – axis, the involved orbitals are p_x , p_z , d_{xy} and d_{yz} . A comparison between the simulation of the $\sigma \rightarrow \pi$ scattered photons and the density of states shows, that the intensity of $\sigma \rightarrow \pi$ scattered photons due to dichroism is maximal for energies with a maximal difference between the density of states of p_x and p_z . In the other hand, the intensity of $\sigma \rightarrow \pi$ scattered photons due to birefringence is maximal for energies where the density of states of p_x and p_z are equal.

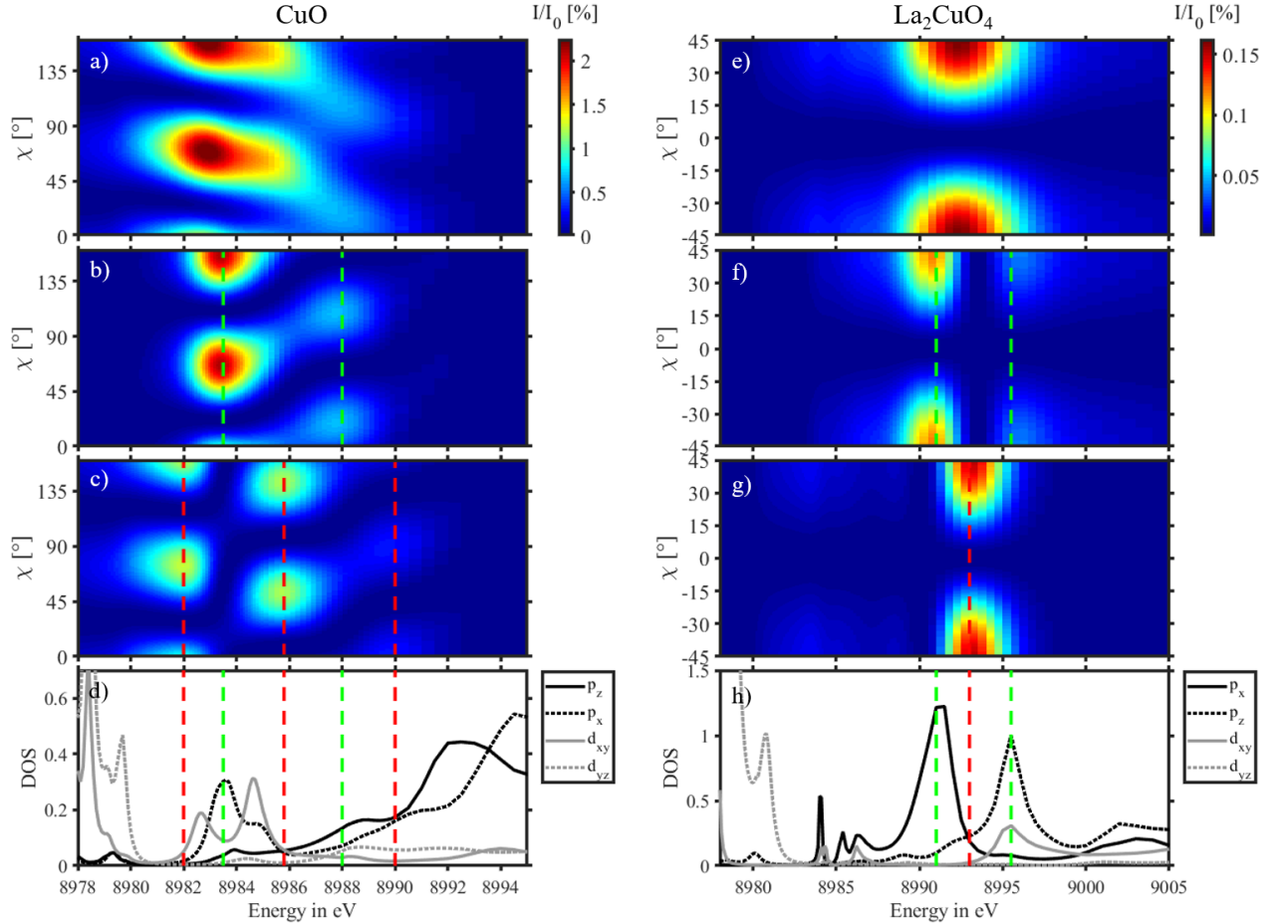


Figure 3. a) Simulated intensity of the $\sigma \rightarrow \pi$ scattered photons of CuO and b) for La₂CuO₄ for different angles χ between the crystal a -axis and the electric field vector. The intensity of the $\sigma \rightarrow \pi$ scattered photons X-ray due to dichroism b) and f), and due to birefringence c) and g) can be attributed to differences between the density of states $\delta(p_x) - \delta(p_z)$ and $\delta(d_{xy}) - \delta(d_{yz})$, respectively. The density of states of the orbitals p_x , p_z , d_{xy} and d_{yz} are shown for CuO in d) and for La₂CuO₄ in h). Maximal difference between the density of p – states leads to dichroism (green lines), while birefringence is maximal at energies, where the density of states of both p – Orbitals are equal (red lines).

-
- [1] S. Asbrink and L.-J. Norrby, *Acta Crystallographica Section B* **26**, 8 (1970).
 - [2] M. Tuilier, B. Chevalier, A. Tressaud, C. Brisson, J. Soubeyroux, and J. Etourneau, *Physica C: Superconductivity* **200**, 113 (1992).
 - [3] C. Brouder, *Journal of Physics: Condensed Matter* **2**, 701 (1990).
 - [4] S. W. Lovesey and S. P. Collins, *Journal of Synchrotron Radiation* **8**, 1065 (2001).
 - [5] S. P. Collins, I. Dolbnya, B. A. Palmer, G. R. Edwards-Gau, A. Morte-Rdenas, B. M. Kariuki, G. K. Lim, K. D. M. Harris, and Y. Joly, *Journal of Physics: Conference Series* **425**, 132015 (2013).
 - [6] Y. Joly, *Phys. Rev. B* **63**, 125120 (2001).